

**Supporting Information:**  
**Intrinsic Lifetime of Higher Order Exciton States in Tungsten diselenide monolayers**

Samuel Brem<sup>1,\*</sup>, Jonas Zipfel<sup>2</sup>, Malte Selig<sup>3</sup>, Archana Raja<sup>4</sup>, Lutz Waldecker<sup>5</sup>, Jonas Ziegler<sup>2</sup>, Takashi Taniguchi<sup>6</sup>, Kenji Watanabe<sup>6</sup>, Alexey Chernikov<sup>2</sup>, and Ermin Malic<sup>1</sup>

<sup>1</sup>*Chalmers University of Technology, Department of Physics, 41296 Gothenburg, Sweden*

<sup>2</sup>*University of Regensburg, Department of Physics, 93053 Regensburg, Germany*

<sup>3</sup>*Technical University Berlin, Institute of Theoretical Physics, 10623 Berlin, Germany*

<sup>4</sup>*Kavli Energy NanoScience Institute, University of California Berkeley, Berkeley, USA*

<sup>5</sup>*Stanford University, 348 Via Pueblo Mall, Stanford, California 94305, USA and*

<sup>6</sup>*National Institute for Materials Science, Tsukuba, Ibaraki 305-004, Japan*

**CONTENTS**

I. Hamilton Operator and Material Parameters	2
II. Wannier Equation and Intervalley Scattering	3
III. Experimental Procedure and Linewidth Extraction	4
IV. Temperature Dependent Spectra	5
References	6

---

\* samuel.brem@chalmers.se

## I. HAMILTON OPERATOR AND MATERIAL PARAMETERS

The properties of the TMD monolayer are described by the following many-particle Hamiltonian:

$$\begin{aligned}
H &= H_0 + H_{\text{Coul}} + H_{\text{el-l}} + H_{\text{el-ph}} \\
&= \sum_{\alpha\mathbf{k}} \varepsilon_{\alpha\mathbf{k}} a_{\alpha\mathbf{k}}^\dagger a_{\alpha\mathbf{k}} + \sum_{\lambda\mathbf{q}} \hbar\omega_{\lambda\mathbf{q}} b_{\lambda\mathbf{q}}^\dagger b_{\lambda\mathbf{q}} \\
&\quad + \frac{1}{2} \sum_{\alpha\beta\mathbf{k}\mathbf{k}'\mathbf{q}} W_{\mathbf{q}} a_{\alpha\mathbf{k}+\mathbf{q}}^\dagger a_{\beta\mathbf{k}'-\mathbf{q}}^\dagger a_{\beta\mathbf{k}'} a_{\alpha\mathbf{k}} \\
&\quad + \frac{e_0}{m_0} \sum_{\alpha\beta\mathbf{k}} \mathbf{M}_{\mathbf{k}}^{\alpha\beta} \cdot \mathbf{A} a_{\alpha\mathbf{k}}^\dagger a_{\beta\mathbf{k}} \\
&\quad + \sum_{\alpha\lambda\mathbf{k}\mathbf{q}} g_{\lambda\mathbf{q}}^{\alpha\mathbf{k}} a_{\alpha\mathbf{k}+\mathbf{q}}^\dagger a_{\alpha\mathbf{k}} (b_{\lambda\mathbf{q}} + b_{\lambda,-\mathbf{q}}^\dagger)
\end{aligned} \tag{1}$$

Here  $a_{\alpha\mathbf{k}}^{(\dagger)}$  denotes the annihilation (creation) operator of an electron in band  $\alpha = c, v$  with momentum  $\mathbf{k}$ , and  $b_{\lambda\mathbf{q}}^{(\dagger)}$  annihilates (creates) a phonon in mode  $\lambda$  with momentum  $\mathbf{q}$ . For the electronic bandstructure  $\varepsilon_{\alpha\mathbf{k}}$  we use the effective mass approximations deduced from ab initio calculation (PBE) in ref. [1], while the phonon dispersion  $\omega_{\lambda\mathbf{q}}$  is described in Debye (long range acoustic) or Einstein approximation (optical and short range acoustic) with sound velocities and energies adopted from DFPT calculations in ref.[2]. For the Coulomb interaction  $W_{\mathbf{q}}$  we derive a modified form of the potential in ref.'s [3, 4] for charges in a thin film of thickness  $d$  surrounded by a dielectric environment. In this work we explicitly take into account anisotropic dielectric tensors. Solving the Poisson equation with the above described boundary conditions yields  $W_{\mathbf{q}} = V_{\mathbf{q}}/\epsilon_{scr}(q)$ , with the bare 2D-Fourier transformed Coulomb potential  $V_{\mathbf{q}}$  and a non-local screening,

$$\epsilon_{scr}(q) = \kappa_1 \tanh\left(\frac{1}{2}[\alpha_1 dq - \ln\left(\frac{\kappa_1 - \kappa_2}{\kappa_1 + \kappa_2}\right)]\right), \tag{3}$$

where  $\kappa_i = \sqrt{\epsilon_i^{\parallel}/\epsilon_i^{\perp}}$  and  $\alpha_i = \sqrt{\epsilon_i^{\parallel}/\epsilon_i^{\perp}}$  account for the parallel and perpendicular component of the dielectric tensor  $\epsilon$  of the monolayer ( $i = 1$ ) and the environment ( $i = 2$ ). The momentum matrix element  $\mathbf{M}_{\mathbf{k}}^{\alpha\beta} = -i\hbar\langle\alpha\mathbf{k}|\nabla|\beta\mathbf{k}\rangle$  is derived from a two band  $k \cdot p$  Hamiltonian, which in vicinity of the K point yields [5]

$$|\mathbf{M}_{\mathbf{k}}^{vc} \cdot \mathbf{e}_{\sigma}|^2 \equiv |M_{\sigma}|^2 = \frac{1}{2} \left[ \frac{a_0 m_0 t}{\hbar} (1 + \sigma) \right]^2. \tag{4}$$

The next neighbor hopping integral  $t = \hbar/a_0 \sqrt{E_g/(m_e + m_h)}$  is determined by the effective masses  $m_{e/h}$  of electrons and holes and the single particle bandgap  $E_g$  at the K-point, while  $\sigma = \pm 1$  for left-(right-)handed circularly polarized light. In Table I we summarize the used parameters for hBN encapsulated WSe<sub>2</sub> for the evaluation of Eq. (3) and (4).

Finally the electron phonon coupling  $g_{\lambda\mathbf{q}}^{\alpha\mathbf{k}}$  is approximated with the generic form of a deformation potential

Parameter	Value	Reference
Lattice constant $a_0$	0.334 nm	[6]
Layer thickness $d$	0.652 nm	[6]
dielec. para. $\epsilon_{WSe_2}^{\parallel}$	15.1	[6]
dielec. perp. $\epsilon_{WSe_2}^{\perp}$	7.5	[6]
dielectr. hBN $\kappa_{hBN}$	4.5	[7]
Bandgap $E_g$ (hBN enc.)	2.38 eV (2.02 eV)	[1, 8]
Electron mass (at K) $m_e$	$0.29m_0$	[1]
Hole mass (at K) $m_h$	$0.36m_0$	[1]

Table I. List of the used parameters for the calculation of exciton eigenenergies and wavefunctions in hBN encapsulated WSe<sub>2</sub> monolayers.

$$g_{\lambda\mathbf{q}}^{\alpha\mathbf{k}} \approx \sqrt{\frac{\hbar}{2\rho A\omega_{\lambda\mathbf{q}}}} D_{\lambda\mathbf{q}}^{\alpha} \quad (5)$$

Here  $\rho$  denotes the surface mass density of the monolayer and  $A$  the area of the system. For the coupling constant  $D_{\lambda\mathbf{q}}^{\alpha}$  we adopt the approximations deduced from DFPT calculations in ref. [2], where long range acoustic phonons couple linear in momentum  $D_{\lambda\mathbf{q}}^{\alpha}|_{\text{intra ac}} \approx D_{\lambda}^{\alpha(1)}q$ , while optical phonons and short range acoustic modes couple with a constant strength  $D_{\lambda\mathbf{q}}^{\alpha}|_{\text{inter ac,opt}} \approx D_{\lambda}^{\alpha(0)}$  in vicinity of high symmetry points. We take into account the LA,TA,LO,TO and A1 mode for intravalley as well as scattering of electrons to the  $\Lambda, \Lambda'$  and  $K'$  valley and hole scattering to the  $\Gamma$  or  $K'$  point. The constants  $D^{(0)}$  and  $D^{(1)}$  for all possible intra and intervalley scattering channels are listed in ref. [2].

## II. WANNIER EQUATION AND INTERVALLEY SCATTERING

The linear optical response of a system is obtained from the Heisenberg equation of motion for the microscopic polarisation  $p_{\mathbf{k}\mathbf{Q}} = \langle a_{c,\mathbf{k}+\alpha\mathbf{Q}}^{\dagger} a_{v,\mathbf{k}-\beta\mathbf{Q}} \rangle$  [9]. We use relative ( $\mathbf{k}$ ) and center-of mass coordinates ( $\mathbf{Q}$ ) with  $\alpha(\beta) = m_{c(v)}/(m_c + m_v)$ . The effective Coulomb interaction between charge carriers in TMDs leads to a strong coupling of polarisations at different relative momenta  $\mathbf{k}$ , yielding an excitonic eigen spectrum for interband transitions. To decouple the equations of motion we perform a basis transformation by expanding the polarisation in terms of exciton wave functions  $p_{\mathbf{k}\mathbf{Q}} = \sum_{\nu} \tilde{\Phi}_{\nu\mathbf{Q}}(\mathbf{k}) P_{\nu\mathbf{Q}}$ . To diagonalize the equations of motion for  $P_{\nu\mathbf{Q}}$ , the basis functions have to fulfill the Wannier equation,

$$(\varepsilon_{c,\mathbf{k}+\alpha\mathbf{Q}} - \varepsilon_{v,\mathbf{k}-\beta\mathbf{Q}}) \tilde{\Phi}_{\nu\mathbf{Q}}(\mathbf{k}) - \sum_{\mathbf{q}} W_{\mathbf{q}} \tilde{\Phi}_{\nu\mathbf{Q}}(\mathbf{k} + \mathbf{q}) = E_{\nu\mathbf{Q}} \tilde{\Phi}_{\nu\mathbf{Q}}(\mathbf{k}). \quad (6)$$

Within the vicinity of minima and maxima of valence and conduction band, we approximate the dispersions quadratically, which allows us to separate relative and center of mass motion. When  $\mathbf{K}_c$  denotes the conduction band valley and  $\mathbf{K}_v$  the valence band valley, we find  $\tilde{\Phi}_{\nu\mathbf{Q}}(\mathbf{k}) = \tilde{\Phi}_{\nu}(\mathbf{k}) = \tilde{\Psi}_{\nu}(\mathbf{k} - \alpha\mathbf{K}_v - \beta\mathbf{K}_c)$ , with  $\tilde{\Psi}$  obeying the effective electron-hole Schroedinger equation,

$$\frac{\hbar^2 k^2}{2m_r} \tilde{\Psi}_{\nu}(\mathbf{k}) - \sum_{\mathbf{q}} W_{\mathbf{q}} \tilde{\Psi}_{\nu}(\mathbf{k} + \mathbf{q}) = E_{\nu}^{\text{bind}} \tilde{\Psi}_{\nu}(\mathbf{k}), \quad (7)$$

where  $m_r = (m_c m_v)/(m_c + m_v)$  is the reduced exciton mass for the corresponding valley masses of electrons ( $m_c$ ) and holes ( $m_v$ ). Furthermore, the parabolic approximation yields  $E_{\nu\mathbf{Q}} = E_{\nu}^{\text{bind}} + \hbar^2(\mathbf{Q} - [\mathbf{K}_c - \mathbf{K}_v])^2/(2[m_c + m_v]) + \varepsilon_{c\mathbf{K}_c} - \varepsilon_{v\mathbf{K}_v}$ . Note, that exciton wavefunctions with different valley configurations are centered at different momenta. Therefore, the exciton form factor for scattering from  $\nu = (n, K - K)$  to  $\mu = (m, K - \Lambda)$  reads

$$\mathcal{F}_{\nu\mu}(\alpha_{\mu}\mathbf{q}) = \sum_{\mathbf{k}} \tilde{\Phi}_{\nu}^*(\mathbf{k}) \tilde{\Phi}_{\mu}(\mathbf{k} + \alpha_{\mu}\mathbf{q}) = \sum_{\mathbf{k}} \tilde{\Psi}_n^*(\mathbf{k}) \tilde{\Psi}_m(\mathbf{k} + \alpha_{\mu}[\mathbf{q} - (\Lambda - K)]) \quad (8)$$

Hence, the wavefunction overlap in Eq. (8) gets maximized for a momentum transfer  $\mathbf{q} = \Lambda - K$  connecting  $K$  and  $\Lambda$  valley, while the overlap for intravalley scattering decreases with growing  $q$ . Furthermore, to account for the complex phase of the electron-phonon coupling, we discard mixed terms in the calculation of the exciton-phonon coupling, i.e.

$$|G_{\lambda\mathbf{q}}^{\nu\mu}|^2 \approx \sum_{\eta=e,h} |g_{\lambda\mathbf{q}}^{\eta} \mathcal{F}_{\nu\mu}(\mathbf{q}_{\eta})|^2, \quad (9)$$

assuming similar weights for polar and non-polar coupling mechanism [10] (e.g. optical deformation potential vs. Froehlich interaction).

### III. EXPERIMENTAL PROCEDURE AND LINEWIDTH EXTRACTION

The studied hBN-encapsulated WSe<sub>2</sub> sample was obtained by mechanical exfoliation of hBN and WSe<sub>2</sub> flakes onto polydimethylsiloxane (PDMS) film and subsequent stacking via stamp transfer [11] onto SiO<sub>2</sub>/Si substrate. First, thin hBN flakes (provided by T. Taniguchi and K. Watanabe, NIMS) were stamped onto a 100°C preheated 295 nm thick SiO<sub>2</sub>/Si substrate at ambient conditions. Then a WSe<sub>2</sub> monolayer was stamped on top of the hBN layer, followed by placing an additional hBN layer on top of the structure at 70°C substrate temperature and ambient conditions. The sample was annealed in high vacuum at 150°C for 4-5 hours after each individual stamping process. The sample was scanned to find large, homogeneous areas of several micrometers with narrow exciton resonances in both light emission and reflectance, indicating successful transfer and good interlayer coupling.

Reflectance measurements were performed using a spectrally broadband tungsten-halogen lamp for illumination. The reflected signals were collected both on the sample ( $R_s$ ) and on the SiO<sub>2</sub>/Si substrate reference ( $R_r$ ), spectrally dispersed in a grating spectrometer, and detected by a cooled CCD camera. The sample was placed in an optical microscopy cryostat cooled by liquid helium. The heat sink temperature was tuned between 4 and 300 K, giving the system sufficient time to reach equilibrium between individual measurements. The lattice temperature of the sample was independently confirmed by the relative energy shift of the exciton resonance.

For the analysis, the acquired reflectance signals are presented in terms of reflectance contrast, defined as  $R_C = (R_s - R_r)/(R_r - R_{bg})$ , where  $R_{bg}$  denotes the background signal without illumination.  $R_C$  thus corresponds to the relative change in the reflectance of the sample with respect to the bare SiO<sub>2</sub>/Si substrate. A representative reflectance contrast spectrum of the WSe<sub>2</sub> monolayer at the temperature of 4 K is shown in Fig. 1 (a). The corresponding first derivative of  $R_C$  with respect to the photon energy is plotted in Fig. 1 (b). In the studied spectral range, the optical response of the sample is dominated by the A exciton ground state resonance (1s) at 1.721 eV, first excited state transition (2s) at 1.853 eV and a weak feature of the second excited state (3s) at 1.876 eV. The absence of pronounced features below the 1s resonance indicate negligible free charge carrier densities.

To extract the exciton peak parameters, the energy-dependent dielectric function of the WSe<sub>2</sub> monolayer  $\varepsilon(E)$  is parameterized with multiple Lorentzian resonances:

$$\varepsilon(E) = \varepsilon_b + \sum_{j=1}^N \frac{f_j}{E_j^2 - E^2 - iE\Gamma_{nr,j}}, \quad (10)$$

where  $f_j$ ,  $E_j$ , and  $\Gamma_{nr,j}$  represent the oscillator strength, peak energy, and the purely *non-radiative* damping of the resonance with the index  $j$ , respectively. The linewidth is defined as full-width-half-maximum of the respective peak

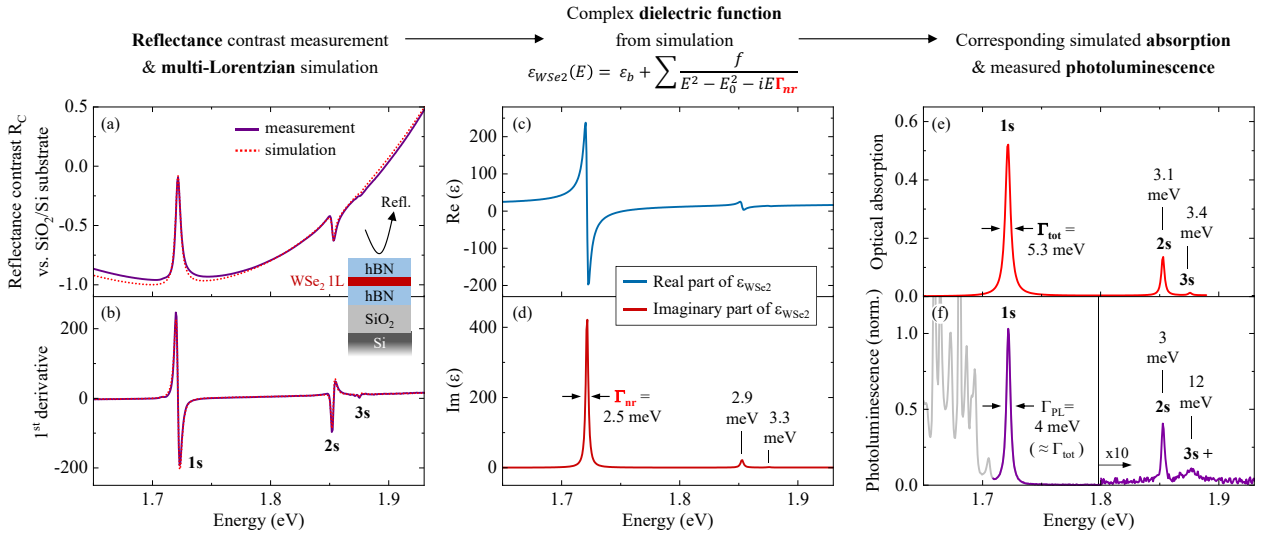


**Figure 1.** (a) Reflectance contrast of the hBN-encapsulated WSe<sub>2</sub> monolayer at 4K together with the simulated spectrum from the multi-Lorentzian model. (b) First-order derivative of the measured and simulated reflectance contrast. (c), (d) Real and imaginary parts of the parameterized dielectric function used in the simulation. In the imaginary part, non-radiative linewidths  $\Gamma_{nr}$  of the ground and the first two excited state exciton transitions are indicated. (e) Corresponding simulated optical absorption spectrum of the  $n = 1, 2, 3$  exciton resonances. Total linewidths are indicated by  $\Gamma_{tot}$ . (f) Measured continuous-wave photoluminescence spectrum of the same sample at 4 K.

in the imaginary part. Only a small number  $N$  of the resonances is included in the simulation. In the spectral range of interest, only those clearly visible in the measured spectra are considered, i.e., the exciton 1s, 2s, and 3s states. The reflectance contrast is then computed using a transfer-matrix formalism [12] taking into account multi-layer interference effects due to the presence of the hBN layers and the SiO<sub>2</sub>/Si substrate. For the studied structure, the thickness of the SiO<sub>2</sub> layer was set to 296 nm and the thickness of the top and bottom hBN layers - to 16.4 nm (using refractive index of 2.2) to obtain the measured overall spectral shape of the reflectance contrast. The exciton peak parameters are then adjusted to match the measured first order derivative. The simulated spectra are presented alongside experimental data in Figs. 1 (a) and (b), exhibiting good agreement and allowing for a reasonable extraction of the exciton peak parameters.

Real and imaginary parts of the dielectric function corresponding to the simulated response are presented in Figs. 1 (c) and (d), respectively. We note, that the width of the resonances in the imaginary part is determined only by the *non-radiative* broadening  $\Gamma_{nr}$ . In contrast to that, *total* linewidths of the same peaks in the optical absorption include additional broadening due to the radiative coupling, i.e., finite oscillator strength. The absorption spectrum computed from the same dielectric function is shown in Fig. 1 (e). For the 1s resonance, in particular, the total linewidth  $\Gamma_{tot}$  of the absorption peak is extracted to be 5.3 meV compared to the purely non-radiative broadening  $\Gamma_{nr}$  of 2.5 meV. Total linewidths are used for comparison with theory throughout the paper.

Here, we note that the resonance linewidths in the emission spectra should also correspond to the total linewidths from absorption, i.e., include both radiative and non-radiative contributions. For comparison, a representative photoluminescence (PL) spectrum obtained at roughly the same position on the WSe<sub>2</sub> sample as the reflectance measurements is shown in Fig. 1 (f). A continuous-wave laser emitting at 532 nm was used for the excitation with a power of 10  $\mu$ W focused to a spot of about 1  $\mu$ m. The emission from the exciton ground and excited states is highlighted in the data. The signals associated with more complex exciton states below the 1s resonance (trions, biexcitons, localized states etc.) are shown in gray. The linewidth of the exciton resonance is found to be in the range of 4-5 meV in PL, close to the values obtained in the absorption spectra.

#### IV. TEMPERATURE DEPENDENT SPECTRA

Experimentally measured reflectance contrast spectra are presented as first derivatives in the Fig. 2 (a) and (b) in the spectral range of ground and excited state resonances, respectively. The simulation results from the multi-Lorentzian peak analysis, discussed in the previous section, are plotted alongside the measured data. Three exciton states, 1s, 2s, and 3s, are observed at 4 K. The 2s state is detected up to room temperature and the 3s state is resolved at 100 K and below. As the temperature increases, the exciton resonances shift to lower energies in good agreement with the literature results on as-exfoliated samples [13]. We note that the shifts of the ground and excited states are very similar, i.e., the shift of the 2s state closely follows that of the 1s resonance with small deviations on the order of several meV towards room temperature. The energy shifts are accompanied by pronounced spectral broadening due to exciton-phonon scattering, analyzed and discussed in the main manuscript in detail.

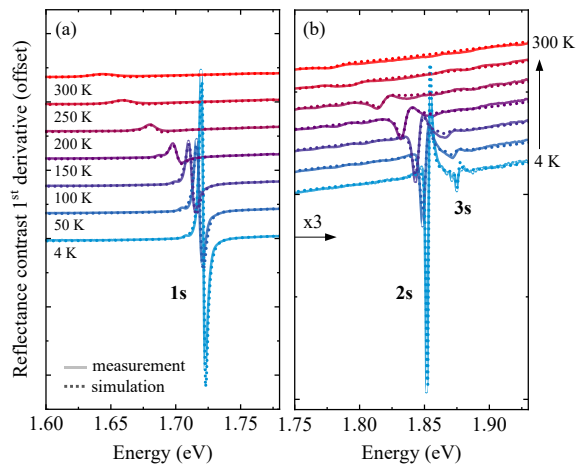


**Figure 2.** (a) Measured reflectance contrast derivatives of the hBN-encapsulated WSe<sub>2</sub> sample for temperatures from 4 to 300 K together with the simulation results. The spectra are presented in the spectral range of the 1s ground state exciton resonance. (b) Same as (a) in the spectral range of excited state resonances. The data are vertically offset for clarity.

- 
- [1] A. Kormányos, G. Burkard, M. Gmitra, J. Fabian, V. Zólyomi, N. D. Drummond, and V. FaláŽko, *2D Materials* **2**, 022001 (2015).
  - [2] Z. Jin, X. Li, J. T. Mullen, and K. W. Kim, *Physical Review B* **90**, 045422 (2014).
  - [3] N. Rytova, *Proc. MSU, Phys., Astron.* **3**, 30 (1967).
  - [4] L. Keldysh, *JETP Lett.* **29**, 658 (1979).
  - [5] D. Xiao, G.-B. Liu, W. Feng, X. Xu, and W. Yao, *Physical Review Letters* **108**, 196802 (2012).
  - [6] A. Laturia, M. L. Van de Put, and W. G. Vandenberghe, *npj 2D Materials and Applications* **2**, 6 (2018).
  - [7] R. Geick, C. Perry, and G. Rupprecht, *Physical Review* **146**, 543 (1966).
  - [8] Y. Cho and T. C. Berkelbach, *Physical Review B* **97**, 041409 (2018).
  - [9] M. Kira and S. Koch, *Progress in quantum electronics* **30**, 155 (2006).
  - [10] K. Kaasbjerg, K. S. Thygesen, and A.-P. Jauho, *Physical Review B* **87**, 235312 (2013).
  - [11] A. Castellanos-Gomez, M. Buscema, R. Molenaar, V. Singh, L. Janssen, H. S. J. van der Zant, and G. A. Steele, *2D Materials* **1**, 11002 (2014), 1311.4829.
  - [12] S. Byrnes, “Multilayer thin film optics calculator, <http://sjbyrnes.com/multilayer-film-optics-programs/>,” (2012).
  - [13] A. Arora, M. Koperski, K. Nogajewski, J. Marcus, C. Faugeras, and M. Potemski, *Nanoscale* **7**, 10421 (2015).